J Mater Sci (2018) 53:13538–13549

Mechanochemical Synthesis

Synthesis of LaB_6–Al_2O_3 nanocomposite powders via ball milling-assisted annealing

Emre Tekoğlu[1,*], Ceren İmer[1], Duygu Ağaoğulları[1], and M. Lütfi Öveçoğlu[1]

[1] *Metallurgical and Materials Engineering Department, Particulate Materials Laboratories (PML), Faculty of Chemical and Metallurgical Engineering, Istanbul Technical University, 34469 Maslak, Istanbul, Turkey*

Received: 7 February 2018
Accepted: 12 May 2018

ABSTRACT

In this study, LaB_6–Al_2O_3 nanocomposite powders were synthesized via ball milling-assisted annealing process starting from La_2O_3–B_2O_3–Al powder blends. High-energy ball milling was conducted at various durations (0, 3, 6 and 9 h). Then, the milled powders were annealed at 1200 °C for 3 h under Ar atmosphere in order to obtain LaB_6 and Al_2O_3 phases as reaction products. X-ray diffractometry (XRD), scanning electron microscopy/energy-dispersive spectrometry (SEM/EDS) and transmission electron microscopy (TEM) techniques were utilized to carry out microstructural characterization of the powders. No reaction between the reactants was observed in the XRD patterns of the milled powders, indicating that high-energy ball milling did not trigger any chemical reactions even after milling for 9 h. $LaAlO_3$ and $LaBO_3$ phases existed in the annealed powders which were milled for 0, 3 and 6 h. $LaBO_3$ phase was removed after HCl leaching. 9-h milled and annealed powders did not exhibit any undesired phases such as $LaAlO_3$ and $LaBO_3$ after leaching step, and pure nanocrystalline LaB_6–Al_2O_3 composite powders were successfully obtained. TEM analyses revealed that very fine LaB_6 particles ($\sim$ 100 nm) were embedded in coarse Al_2O_3 ($\sim$ 500 nm) particles.

Introduction

Aluminum oxide (Al_2O_3) has attractive properties such as high hardness, high wear resistance, high chemical stability and good thermal conductivity [1, 2]. Besides being a cost-effective and readily available material, Al_2O_3 is an important engineering ceramic widely used in cutting tools, biomedical materials, electrical insulators and as reinforcing particles in metal matrix composites [3–6]. On the other hand, lanthanum hexaboride (LaB_6) is a transition metal boride exhibiting excellent properties such as high melting temperature, high strength, high hardness, high chemical and thermal stability, low electronic work function and low thermal expansion coefficient [7, 8]. LaB_6 has unique application areas compared to Al_2O_3 due to its distinctive electronic structure, and magnetic, optical and thermionic properties [9–11].

Address correspondence to E-mail: tekoglue@itu.edu.tr

https://doi.org/10.1007/s10853-018-2454-6

Lanthanum hexaboride is generally synthesized by using several high-temperature processes including floating zone method [12–14], chemical vapor deposition [15, 16], carbothermal reduction [17], solid-state reactions [18, 19] and liquid-state reactions [14]. Apart from these techniques, mechanochemical synthesis (MCS) is an alternative process for obtaining nanocrystalline LaB_6 powders [20, 21]. MCS is a solid-state synthesis method in which new phases emerge as a result of reactions between starting powders within the welding, breaking and rewelding cycles in a high-energy ball mill [22–24]. Due to the intensive plastic deformation in the milling media, starting powders comprise a high amount of material defects such as stacking faults, dislocations, vacancies, etc., and hence, the activation energy required to proceed the exchange reactions is significantly reduced [25, 26]. If new phases are synthesized in situ during high-energy ball milling, the process is named as MCS. On the other hand, if they are obtained after short-time high-energy ball milling followed by annealing, the process is designated as mechanically activated annealing [27, 28]. In addition, long-time high-energy ball milling and annealing process can be applied for the emergence of new phases [29, 30]. It has been shown that the combination of ball milling and annealing is an effective route in producing various refractory materials [24]. Ağaoğulları et al. [20] synthesized LaB_6 and MgO powders from La_2O_3, B_2O_3 and Mg initial materials by a mechanochemical reaction in a high-energy ball mill. They showed that magnesiothermic reduction took place after milling for 2 h 45 min which yielded LaB_6 and MgO phases and high purity LaB_6 powders were obtained after HCl leaching [20]. Similarly, pure LaB_6 powders were obtained after calciothermic reduction in La_2O_3 and B_2O_3 in a high-energy ball mill by MCS for 2 h and after a purification step [21]. Besides, Akgün et al. [31] achieved nano-scaled LaB_6 powders after MCS in a high-energy ball mill. However, there is an open area in the archival literature about the facile synthesis of LaB_6 powders embedded in an oxide ceramic material. It should be also noted that almost no available investigations exist regarding the solid-state synthesis of LaB_6–Al_2O_3 powders in the literature that provide potential applications. However, some attempts were made for the solid-state synthesis of Al_2O_3–TiB_2, Al_2O_3–ZrB_2, Al_2O_3–NbB_2, etc. [32–34]. Additionally, it has been reported that transition borides such as TiB_2, ZrB_2 and NbB_2 enhanced the mechanical properties of the Al_2O_3-based composites in terms of fracture toughness, hardness, etc. [33, 35, 36]. The LaB_6–Al_2O_3 ceramic powders can be suitable candidates as particulate reinforcements and they can contribute to the microstructural and/or mechanical properties of the ceramic or metallic matrix composites.

In the present study, pure LaB_6–Al_2O_3 nanocomposite powders were synthesized by a combined method of high-energy ball milling, annealing and leaching processes for the first time in the archival literature. The effect of milling time on the formation of LaB_6 and Al_2O_3 phases were investigated in terms of detailed microstructural characterizations.

Experimental procedure

La_2O_3 (Alfa Aesar^{TM}, 99.99% purity) and B_2O_3 (ETI Mine, 98% purity) powders were used as oxide starting materials. Al (Alfa Aesar^{TM}, 99.5% purity) powders were utilized as metallic reducing agent. Particle size analysis (PSA) of the raw materials was conducted in a Malvern^{TM} Mastersizer 2000 particle analyzer using distilled water as the aqueous media. Microstructural characterization of the powders was carried out using a JEOL^{TM} JCM-6000Plus NeoScope scanning electron microscope (SEM, operated at 15 kV) and its coupled energy-dispersive spectrometer (EDS). Figure 1a–f shows the representative SEM micrographs and corresponding particle size distributions of the La_2O_3, B_2O_3 and Al initial powders which have mean particle sizes of 10.1, 336.6 and 20.2 µm, respectively.

Powder blends containing stoichiometric amounts of reactants were prepared according to the overall reaction given in Eq. (1).

$$La_2O_3 + 6B_2O_3 + 14Al = 2LaB_6 + 7Al_2O_3. \qquad (1)$$

For each run, powder batches of 8 g (2.32 g La_2O_3, 2.98 g B_2O_3 and 2.70 g Al) were weighed in a Precisa^{TM} XB320 M sensitive balance (precision: 0.001 g). Ball milling experiments were carried out in a Spex^{TM} 8000D Mixer/Mill having a clamp speed of 1060 cycles/minute (115 V) with a ball-to-powder weight ratio (BPR) of 10:1 using hardened steel balls (a total of 60 milling balls each with a diameter of 6 mm) in a hardened steel vial (50 ml capacity). It should be mentioned that prior to the milling experiments, powder blends, milling vials and milling balls were

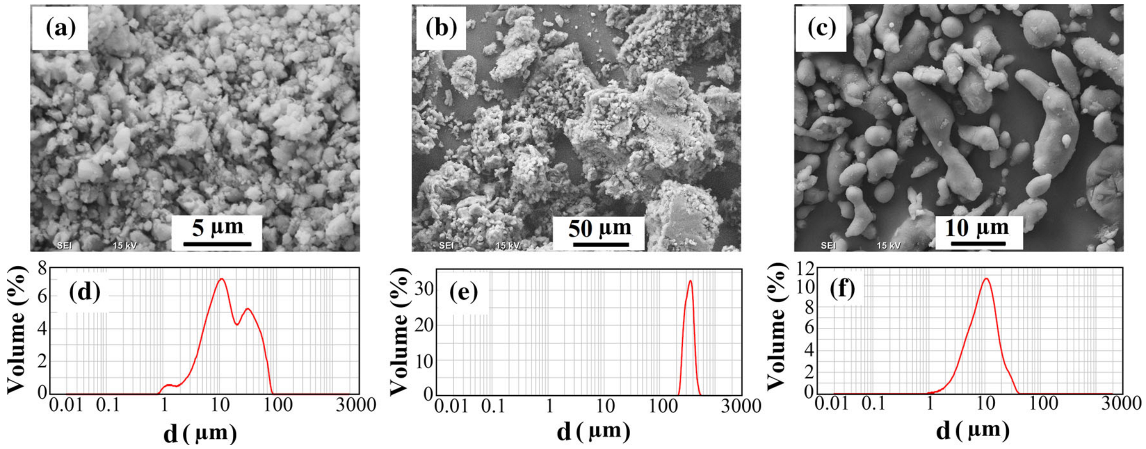

Figure 1 SEM and PSA images of the raw materials **a**, **d** La_2O_3, **b**, **e** B_2O_3 and **c**, **f** Al.

dried in a vacuum oven at 120 °C for 2 h in order to remove possible moisture adhered on their surfaces. Afterward, the milling vials were evacuated to about 10^{-2} Pa and backfilled with Ar gas (Linde^{TM}, 99.999% purity) in a Plaslabs^{TM} glove-box to prevent surface oxidation/contamination of the powder particles. After sealing the vials, milling was conducted at different durations of 3, 6 and 9 h. Milled powders were unloaded again under Ar atmosphere in the glove-box. Then, powders were compacted into pellets using a hand press located inside the glove-box in order to avoid internal oxidation prior to cold pressing step. On the other hand, non-milled (0 h) powders were blended and homogenized in a WAB^{TM} T2C Turbula blender for 1 h and they are hereafter referred to as-blended powders. Before annealing process, hand-pressed pellets were compacted in a 10-ton capacity MSE^{TM} MP-0710 uniaxial hydraulic press under a pressure of 450 MPa. The reason for compacting the powders was to increase the contact area between them and hence to increase atomic diffusion rate to produce the desired phases. The compacted green bodies were placed in an alumina boat in a Linn^{TM} HT-1800 high-temperature controlled-atmosphere furnace and annealed at 1200 °C for 3 h with a heating and cooling rate of 5 °C under Ar gas flow. Annealed samples were easily ground in a mortar before the purification step in order to obtain powders free from agglomeration for an effective leaching. Selective HCl (Merck^{TM}, 37% concentrated) leaching of the annealed samples were conducted in an ultrasonic bath (Bandelin^{TM} Sonorex) with the help of ultrasonic stirring. Leaching was carried out with the aim of removing the undesired $LaBO_3$ phase and the impurities (Fe, Ni, Cr) released from the milling media. The leaching parameters such as concentration, solid-to-liquid ratio of the solution and duration were selected as 6 M, 1 g/10 cm^3 and 15 min, respectively. The solutions containing insoluble solids were centrifuged (Hettich^{TM} centrifuge, at 3500 rpm for 25 min), the supernatant liquid was decanted, and residual solids were washed with distilled water for three times. Residual solids were dried in air (FN 500 stove, at 100 °C for 12 h).

The standard Gibbs free energy change ($\Delta G°$) and standard enthalpy change ($\Delta H°$) versus temperature curves were plotted using HSC Chemistry^{TM} Ver. 9.0.7 program. The crystalline phases of the powders were identified using a Bruker^{TM} D8 Advanced Series X-ray diffractometer (XRD) using CuK_α (1.54060 Å) radiation in the 2θ range of 10–90° with a scanning rate of 5°/min. International Center for Diffraction Data® (ICDD) powder diffraction files were utilized for the identification of crystalline phases. Average crystallite sizes and lattice strains of the Al in the milled powders and those of the LaB_6 and Al_2O_3 in the annealed powders were predicted using the Williamson–Hall method and Lorentzian rule using a Bruker^{TM}-AXS TOPAS 4.2 software. Williamson–Hall equation is expressed as Eq. (2) below [37] [37];

$$\beta_{hkl} \cos \theta_{hkl} = \left(\frac{k\lambda}{D}\right) + 4\varepsilon \sin \theta_{hkl} \tag{2}$$

where β_{hkl} is the full width half maximum (FWHM), D is crystallite size, k is shape factor ($\approx$ 0.9), and λ is wavelength of the CuK_α radiation and ε is the lattice strain.

Milled powders were also subjected to particle size measurements using a Microtrac^{TM} Nano-Flex particle size analyzer. Detailed microstructural analyses were conducted on the powders using a JEOL^{TM} JEM-2100 transmission electron microscope (TEM) operated at 200 kV.

Results and discussion

Thermodynamic calculations

In addition to the overall reaction in Eq. (1) which yielded the main products such as LaB_6 and Al_2O_3, the probable reactions with the formation of $LaAlO_3$ and $LaBO_3$ by-products are given in Eqs. (3) and (4). The standard Gibbs free energy and enthalpy changes of the reactions in Eqs. (1), (3) and (4) were calculated by HSC Chemistry^{TM} Ver. 9.0.7 as a function of temperature, as shown in Fig. 2a, b, respectively. It is clear that all these three reactions have large negative free energy changes between 25 and 1500 °C (Fig. 2a). Additionally, standard enthalpy changes of the relevant reactions indicate a large amount of heat release (Fig. 2b) due to the intense exothermic reactions triggered by Al. The calculated $\Delta G°$ values of Eqs. (1), (3) and (4) at 25°C were determined as − 2504.95, − 1312.73 and − 1192.22 kJ, respectively. Thermodynamic calculations obtained from thermite-type reactions belonging to La_2O_3–B_2O_3–Ca and La_2O_3–B_2O_3–Mg systems were previously reported by Ağaoğulları et al. [20, 21]. According to the La_2O_3–B_2O_3–Ca system, calciothermic reaction has a large negative free energy change between − 4050 and − 2700 kJ and a large enthalpy change between − 4150 and − 4500 kJ in the temperature range of 0–2000 °C [21]. According to the La_2O_3–B_2O_3–Mg system, magnesiothermic reaction has a large negative free energy change between − 3300 and − 1700 kJ and a large enthalpy change between − 3440 and − 3930 kJ in the temperature range of 0–2000 °C [20]. Based on the aluminothermic reaction shown in Eq. (1) in the present study, reaction has a negative free energy change between − 2400 and − 1410 kJ and an enthalpy change between − 2500 and − 2940 kJ, in the temperature range of 0–1500 °C. Besides, the linear regions of the enthalpy change-temperature curve for the La_2O_3–B_2O_3–Al system arise from the melting of B_2O_3 at 450 °C and the melting of Al at 660 °C. It is clearly understood that the calciothermic and magnesiothermic reductions in La_2O_3 and B_2O_3 are more favorable than their aluminothermic reduction. Additionally, Ağaoğulları et al. proved that the thermite-type reactions in the La_2O_3–B_2O_3–Ca and La_2O_3–B_2O_3–Mg systems took place via MCS mechanism during milling without applying an external heat [20, 21]. It can be said that according to the thermodynamic calculations, the use of Al instead of Ca and Mg as a reductant seems to require more energy for the reduction reaction. This means that the thermite-type reaction of La_2O_3–B_2O_3–Al system cannot take place during milling and it needs an external energy. On the other hand, $LaAlO_3$ phase is an undesired reaction product as seen in Eq. (3), it can be subsequently removed by the reaction in Eq. (4). Also, the reaction in Eq. (4) has the

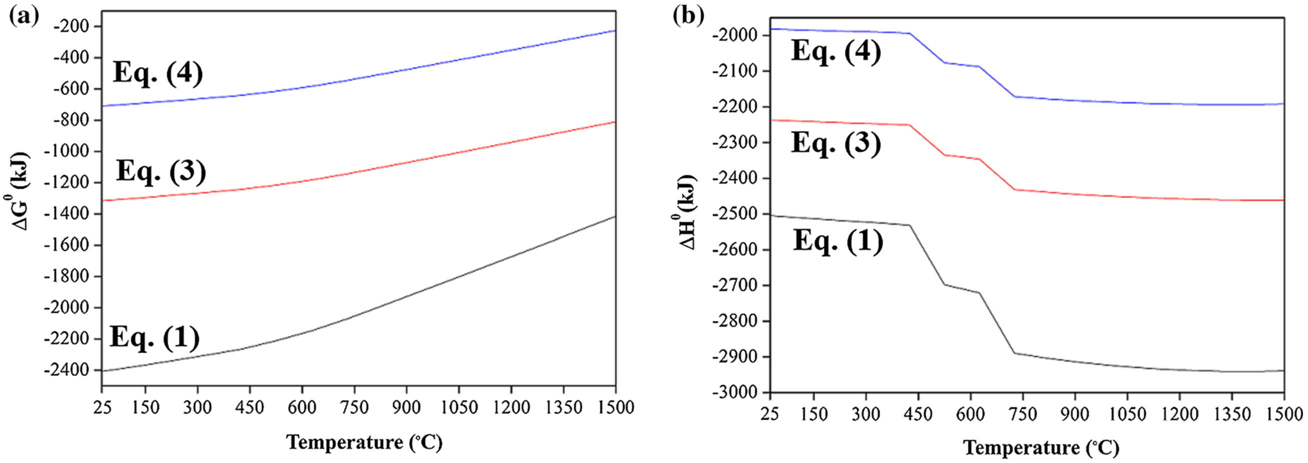

Figure 2 **a** Standard Gibbs free energy change and **b** standard enthalpy change versus temperature curves of the reactions given in Eqs. (1), (3) and (4).

highest $\Delta G°$ value up to 1500 °C among the exothermic reactions, which means that it is less possible to take place among Eqs. (1), (3) and (4) in the same process conditions. Besides, Ağaoğulları et al. [20, 21] demonstrated the emergence of $LaBO_3$ phase together with LaB_6 as a result of the reactions between La_2O_3 and B_2O_3 during high-energy ball milling (Eq. (5)). However, it should be noted that $LaBO_3$ could be easily removed from the powder products by leaching process using highly concentrated HCl solution [20, 21].

$$La_2O_3 + 3B_2O_3 + 7Al = LaAlO_3 + 3Al_2O_3 + LaB_6 \quad (3)$$

$$LaAlO_3 + 3B_2O_3 + 7Al = LaB_6 + 4Al_2O_3 \quad (4)$$

$$La_2O_3 + B_2O_3 = 2LaBO_3. \quad (5)$$

Characterization of the milled powders

Figure 3 illustrates the XRD patterns of the as-blended La_2O_3–B_2O_3–Al powders and those milled at different durations (3, 6 and 9 h). It is evident from Fig. 3 that no reaction took place between the initial particles even after high-energy ball milling for 9 h. All the milled powders have La_2O_3 (ICDD Card No: 71-5408, Bravais lattice: primitive hexagonal, $a = b = 0.393$ nm, $c = 0.614$ nm), B_2O_3 (ICDD Card No: 76-1655, Bravais lattice: primitive hexagonal, $a = b = 0.433$ nm, $c = 0.839$ nm) and Al (ICDD Card No: 004-0787, Bravais lattice: face-centered cubic, $a = b = c = 0.4049$ nm) phases. Besides, the intensities of the La_2O_3, Al and B_2O_3 peaks decreased with increasing milling durations due to continuous collisions and deformation during milling. Previously, Ağaoğulları et al. [20, 21] revealed the synthesis of LaB_6 from La_2O_3 to B_2O_3 starting materials during high-energy ball milling in the presence of Mg- or Ca-reducing agents. However, in the present study, aluminothermic reduction did not occur in the La_2O_3 and B_2O_3 containing blends. In other words, MCS did not take place when Al was used as the reductant instead of Mg or Ca, which is in good agreement with their calculated $\Delta G°$ and $\Delta H°$ values. Furthermore, the type of the present phases did not differ from each other in the milled powders, and especially, Al phase exhibited lower peak intensities for the extended milling times (6 and 9 h).

It is important to mention that especially the intensity of the XRD patterns belonging to the Al phase in Fig. 3 decreases and their widths broaden with increasing milling durations. This can be attributed to decrease in the average crystallite size and increase in the average lattice strain of the Al phase in the milled powders (Table 1). It is well known that defects such as dislocations, vacancies, stacking faults, etc. occur in the microstructure due to

Figure 3 XRD patterns of the as-blended (ab) La_2O_3–B_2O_3–Al powders and those milled at different durations.

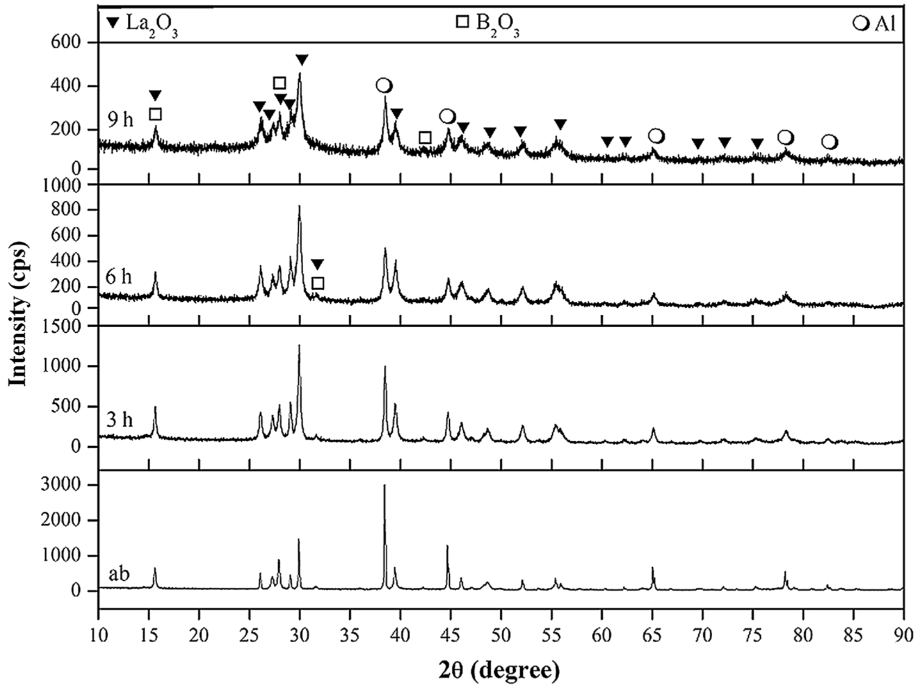

Table 1 Average crystallite sizes and lattice strains of the Al phase in the as-blended and milled powders

Milling time (h)	Average crystallite size (nm)	Average lattice strain (%)
0	420.2	0.0109
3	81.4	0.3317
6	66.9	0.4275
9	50.1	0.6124

intensive plastic deformation during high-energy milling environment [24]. Thus, extended milling durations cause the dislocation densities and the lattice strain amounts to increase. Besides, dynamic recovery exists throughout these defects which leads to recrystallization of sub-grains during high-energy milling [38]. Thus, not only increase in lattice strain but also decrease in crystallite size is inevitable with increasing milling durations.

Figure 4a–h shows the SEM and PSA images of the as-blended La_2O_3–B_2O_3–Al powders and those milled at different durations. As shown in Fig. 4a, as-blended powders consist of white small and dark gray large particles. EDS measurements taken from the white small particles (Region 1) yield the composition of 25.85 ± 2.74 wt% B, 51.68 ± 3.85 wt% O, 22.47 ± 2.17 wt% La, indicating the presence of B_2O_3 and La_2O_3 phases. EDS spectral analysis of 99.88 ± 0.04 wt% Al and ~ 0.12 wt% O (from surface oxidation) taken from the dark gray large particles (Region 2) reveals that these particles are pure Al particles. Since as-blended powders have non-homogeneous microstructural morphology, milled powders have an incorporated microstructure (Fig. 4b–d). Moreover, as-blended powders have a mean particle size of 13.2 µm (Fig. 4e). Particle size analysis of the powders also reveals the gradual contribution of milling on the mean particle size (Fig. 4e–h). On the other hand, 3-h milled powders represent a narrow particle size distribution with a mean particle size of 378 nm (Fig. 4f). However, after milling for 6 h, particle size distribution of the powders became bimodal with two peak points (423 and 136.3 nm) with an average particle size of 374 nm (Fig. 4g). Finally, powders milled for 9 h also have a bimodal particle size distribution (135.4 nm and 366 nm) with a mean particle size of 238.3 nm (Fig. 4h).

General EDS analyses were performed on the as-blended La_2O_3–B_2O_3–Al powders and those milled at different durations (Table 2). Probable Fe contamination released from the milling media was detected from the milled powders. According to the EDS results, the amount of Fe increased as milling time increased from 3 to 9 h. However, the Fe impurity contents can be regarded within the tolerance limits since its highest amount is only 0.23 wt% in the powders milled for 9 h.

Characterization of the annealed and leached powders

Figure 5 shows the XRD patterns of the as-blended La_2O_3–B_2O_3–Al powders and those milled for 3, 6 and 9 h after annealing for 3 h at 1200 °C. Since Eq. (1) does not take place during milling and it requires external heat, the annealing process was carried out for the formation of LaB_6 and Al_2O_3 phases after high-energy ball milling of powder blends. It is well known that diffusion takes place

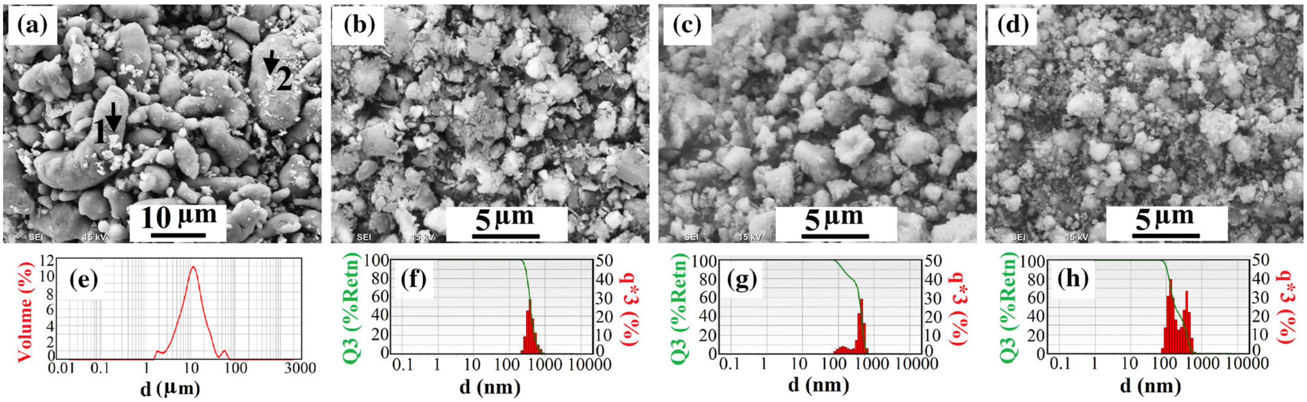

Figure 4 SEM and PSA images of the as-blended La_2O_3–B_2O_3–Al powders and those milled at different durations: **a**, **e** ab, **b**, **f** 3 h, **c**, **g** 6 h and **d**, **h** 9 h.

Table 2 General EDS analyses taken from the as-blended (0 h) La_2O_3–B_2O_3–Al powders and those milled at different durations

Milling time (h)	B (wt%)	O (wt%)	Al (wt%)	La (wt%)	Fe (wt%)
0	16.24	19.14	50.14	14.48	–
3	15.65	18.73	49.75	15.87	0.09
6	15.61	18.57	49.80	16.02	0.22
9	14.82	18.14	51.48	15.56	0.23

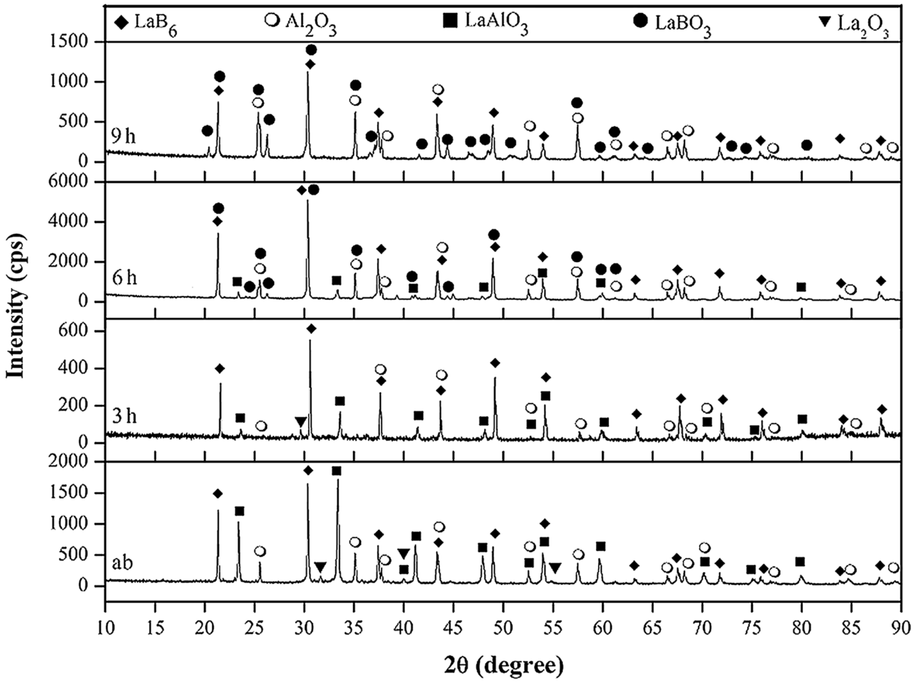

Figure 5 XRD patterns of the as-blended (ab) La_2O_3–B_2O_3–Al powders and those milled for 3, 6 and 9 h followed by annealing.

throughout the defects existing in the microstructure. In this context, increasing milling duration led an increase in the defects and hence free energy barrier of the reactions was decreased and diffusion rate was increased [38]. Contrary to the XRD analyses of the as-blended and milled powders, annealed powders exhibited new phases, indicating that the reduction reactions occurred by the effect of heat. XRD patterns of all the annealed samples show LaB_6 (ICDD Card No: 034-0427, Bravais lattice: primitive cubic, $a = b = c = 0.4156$ nm) and Al_2O_3 (ICDD Card No: 046-1212, Bravais lattice: primitive rhombohedral, $a = b = 0.4476$ nm, $c = 1.2992$ nm) phases. There is a very small indication of unreacted La_2O_3 phase in the as-blended, and 3-h milled and annealed powders. This points out that some amount of La_2O_3 was not incorporated into reactions during annealing probably due to its relatively non-homogeneous distribution in the microstructure compared to those milled at longer durations. Besides, XRD peaks belonging to $LaAlO_3$ phase (ICDD Card No: 031-0022, Bravais lattice: primitive rhombohedral, $a = b = 0.5364$ nm, $c = 1.3110$ nm) was observed in the annealed samples, excepting the 9-h milled and annealed powders. Surprisingly, high amount of $LaAlO_3$ phase present in the as-blended and annealed powders gradually decreased as milling time increased and it disappeared in the annealed powders milled for 9 h. Phases occurred during annealing are in agreement with the product phases predicted by Eqs. (1), (3) and (4). XRD patterns reveal that Eqs. (1) and (3) have taken place and LaB_6, Al_2O_3 and $LaAlO_3$ phases have formed during annealing of the as-blended, 3- and 6-h milled powders. However, 9 h of milling time inhibited the emergence of $LaAlO_3$ phase probably in regard to Eq. (4). Moreover, the $LaBO_3$ phase (ICDD Card No: 012-0762, Bravais lattice: primitive orthorhombic, $a = 0.5130$ nm, $b = 0.8300$ nm, $c = 0.5880$ nm) is the only one observed in the XRD patterns of the 6 and 9 h of milled and annealed powders. Thus, 9-h milled and annealed powders comprise only the LaB_6, Al_2O_3 and $LaBO_3$ phases.

Table 3 Average crystallite sizes and lattice strains of the Al_2O_3 and LaB_6 phases in the as-blended and milled powders followed by annealing

Milling time (h)	Average crystallite size (nm)		Average lattice strain (%)	
	LaB_6	Al_2O_3	LaB_6	Al_2O_3
0	628.8	564.1	0.0076	0.0052
3	306.6	357.6	0.0468	0.0994
6	180.7	253.5	0.0746	0.0177
9	169.4	211.9	0.0885	0.0658

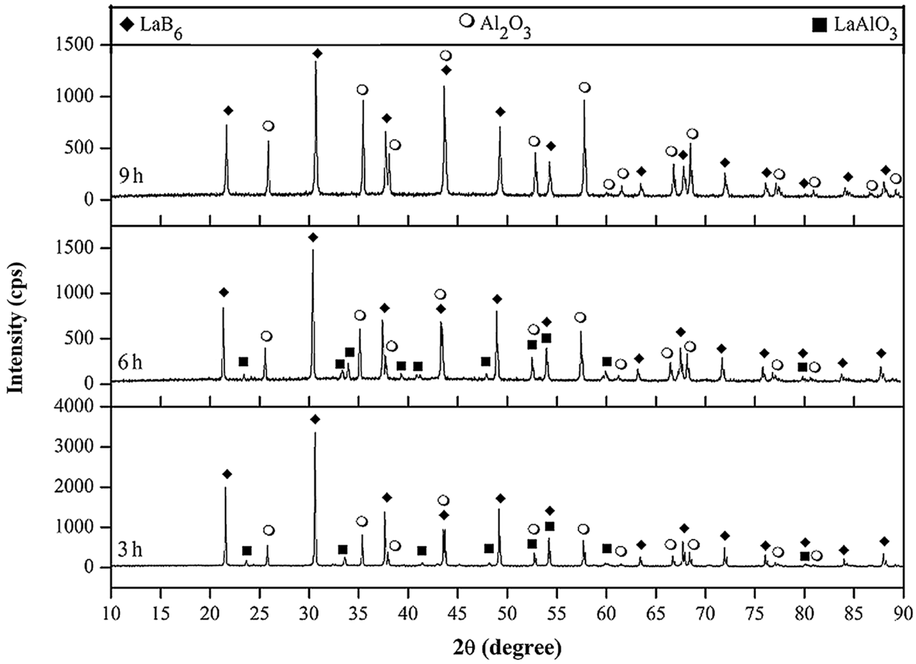

Figure 6 XRD patterns of the La_2O_3–B_2O_3–Al powders and those milled for 3, 6 and 9 h followed by annealing and leaching.

Table 3 shows the average crystallite sizes and lattice strains of the Al_2O_3 and LaB_6 phases in the as-blended and milled powders after annealing. Average crystallite sizes of the Al_2O_3 and LaB_6 phases decreased and their lattice strain values increased as milling time increased. As expected, there is some amount of grain growth during annealing.

Figure 6 displays the XRD patterns of the milled (for 3, 6 and 9 h) La_2O_3–B_2O_3–Al powders after annealing and leaching. It is obvious from Fig. 6 that the $LaBO_3$ phase was completely removed by leaching process. However, there is still some $LaAlO_3$ in the 3 and 6 h of milled, annealed and leached powders. But only after 9 h of milling followed by annealing and leaching, the powders could be successfully synthesized with LaB_6 and Al_2O_3 phases free from undesired by-products.

Figure 7 illustrates the SEM images (a–d) and EDS analyses (e–f) of the as-blended powders and those milled for 3, 6 and 9 h followed by annealing and leaching. It is useful to remind that the annealed powders were ground in mortar for obtaining an effective leaching process. The resultant products were in powder form after leaching process. SEM micrographs showed that particle sizes of the powders tended to decrease by increasing milling duration. As compared the SEM micrographs in Fig. 7a, b with Fig. 7c, d, particles in the as-blended and 3 h of milled, annealed and leached powders were coarser in size than those milled for prolonged durations (6 and 9 h). Besides, irregular-shaped Al_2O_3 particles were smaller and brighter than LaB_6 particles. EDS spectrum (Fig. 7e) taken on the cube-like particle (red-arrowed) in Fig. 7b gives the signals of La and B elements, revealing the presence of LaB_6 particle. Additionally, EDS analysis (Fig. 7f) of the red-arrowed bright and irregular-shaped particle in Fig. 7b shows the signals of Al and O, corresponding to the Al_2O_3 particle. It is evident that brittle LaB_6 and Al_2O_3 powders fracture efficiently during high-

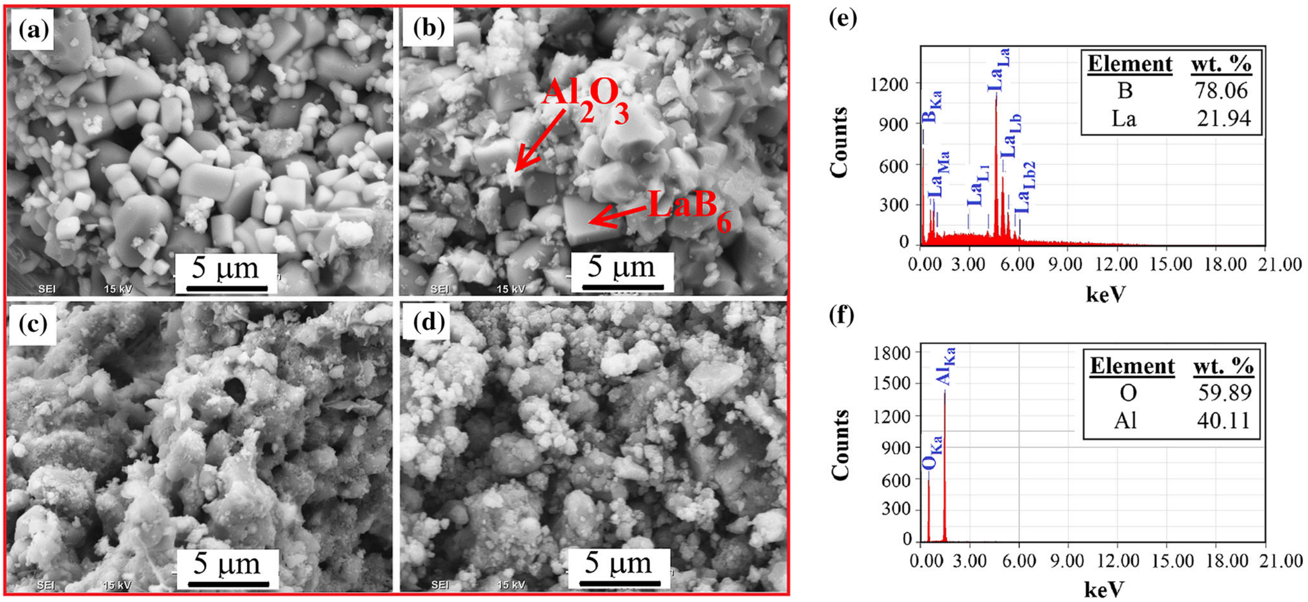

Figure 7 SEM images (**a**–**d**) and EDS analyses (**e**–**f**) of the annealed and leached powders milled at different durations: **a** ab, **b** 3 h, **c** 6 h, **d** 9 h, and **e** EDS spectrum taken from the SEM image in (**b**), revealing the presence of LaB_6 particle and **f** EDS spectrum taken from the SEM image in (**b**), revealing the presence of Al_2O_3 particle.

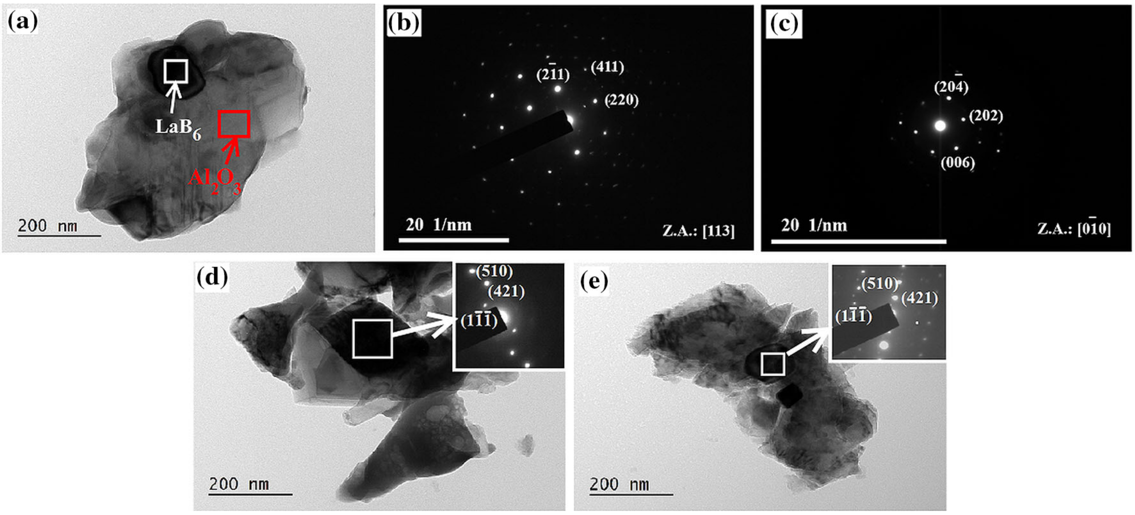

Figure 8 TEM image of the 9 h milled, annealed and leached powders: **a** bright-field (BF) image, **b** selected area diffraction pattern (SADP) taken from the white-squared region in (**a**), showing the presence of LaB_6, and **c** SADP taken from the red-squared region in (**a**), showing the presence of Al_2O_3, and **d**–**e** BF images and SADPs of white-squared regions.

energy ball milling and hence particle sizes significantly decrease [20, 39]. The powders milled for extended durations (6 and 9 h) are not only smaller in size, but also exhibit a well-mixed microstructure (Fig. 7c, d). It is clear that smaller particles have more contact area between their surfaces, and thereby, they tend to agglomerate with each other.

Bright-field (BF) TEM images of 9-h milled, annealed and leached powders, and their corresponding SADPs are shown in Fig. 8a–e. TEM micrograph in Fig. 8a exhibits dark particles (~ 100 nm) embedded in a coarse bright particle in size of about 500 nm. SADPs obtained from the dark region (white-squared) and bright region (red-squared) are, respectively, indexed as shown in Fig. 8b, c, proving that these regions belong to the LaB_6 and Al_2O_3 phases. Moreover, Fig. 8d, e shows the representative BF images including nano-scaled dark regions and their corresponding SADPs which once more reveal the presence of LaB_6 particles with the same zone axis of $[1\bar{5}6]$.

In overall, a simple way of synthesizing LaB_6–Al_2O_3 nanocomposites was carried out using high-energy ball milling, annealing and leaching processes. Long-time-milling-assisted heat treatment and a purification step could be applied to obtain pure boride-oxide systems which are free from undesired secondary phases for some refractory applications at elevated temperatures.

Conclusions

In this study, LaB_6–Al_2O_3 nanocomposites were successfully synthesized via a combined method of high-energy ball milling, annealing and leaching processes. Based on the results reported in the present study, the following conclusions can be drawn:

- Consistent with the thermodynamic predictions of the aluminothermic reactions of the present study, mechanochemical synthesis of the LaB_6 and Al_2O_3 phases did not take place even during milling durations of 9 h. Therefore, subsequent annealing and leaching steps were carried out.
- XRD studies revealed that, in the absence of the undesired phases of $LaAlO_3$ and $LaBO_3$, LaB_6 and Al_2O_3 phases were synthesized after high-energy ball milling for 9 h followed by annealing and leaching.
- SEM micrographs revealed that the particle sizes of the powders dramatically decreased with increasing milling durations. LaB_6 particles were observed with cube-like morphologies.
- Very fine LaB_6 particles ($\sim$ 100 nm) embedded in the coarse Al_2O_3 ($\sim$ 500 nm) particles were observed in the TEM micrographs of the 9-h milled, annealed and leached sample. The formation of the LaB_6 and Al_2O_3 phases was verified by the pertinent SADPs.

Acknowledgements

This study was financially supported by The Scientific and Technological Research Council of Turkey (TUBITAK) through a research project (# 214M093). We also acknowledge Prof. Dr. Cüneyt Arslan and M.Sc. Emre Yılmaz for their assistance in using the HSC Chemistry^{TM} Ver. 9.0.7 program.

Funding

This study was funded by "The Scientific and Technological Research Council of Turkey (TÜBİTAK)" with the project number 214M093.

Compliance with ethical standards

Conflict of interest The authors declare that they have no conflict of interest.

References

[1] Shi XL, Xu FM, Zhang ZJ et al (2010) Mechanical properties of hot-pressed Al_2O_3/SiC composites. Mater Sci Eng, A 527:4646–4649. https://doi.org/10.1016/j.msea.2010.03.035

[2] Hosseini SN, Karimzadeh F, Enayati MH (2012) Mechanochemical synthesis of Al_2O_3/Co nanocomposite by aluminothermic reaction. Adv Powder Technol 23:334–337. https://doi.org/10.1016/j.apt.2011.04.008

[3] Nikkhah AJ, Torabi O, Ebrahimi-Kahrizsangi R et al (2014) Investigation on mechanochemical synthesis of Al2O 3/BN nanocomposite by aluminothermic reaction. Ceram Int 40:5559–5566. https://doi.org/10.1016/j.ceramint.2013.10.147

[4] Palmero P, Kern F, Sommer F et al (2014) Issues in nanocomposite ceramic engineering: focus on processing and properties of alumina-based composites. J Appl Biomater Funct Mater. https://doi.org/10.5301/jabfm.5000185

[5] Mozalev A, Sakairi M, Takahashi H et al (2014) Nanostructured anodic-alumina-based dielectrics for high-frequency integral capacitors. Thin Solid Films 550:486–494. https://doi.org/10.1016/j.tsf.2012.02.077

[6] Reddy MP, Ubaid F, Shakoor RA et al (2017) Effect of reinforcement concentration on the properties of hot extruded Al–Al_2O_3 composites synthesized through microwave sintering process. Mater Sci Eng A 696:60–69. https://doi.org/10.1016/j.msea.2017.04.064

[7] Lihong B, Wurentuya Wei W, Tegus O (2014) A new route for the synthesis of submicron-sized LaB_6. Mater Charact 97:69–73. https://doi.org/10.1016/j.matchar.2014.08.011

[8] Xu J, Min G Hui, Hu L Jie, et al. (2009) Dependence of characteristics of LaB_6 films on DC magnetron sputtering power. Trans Nonferrous Met Soc China (English Ed

19:952–955. https://doi.org/10.1016/s1003-6326(08)60384-2

[9] Kitamura K, Osaka T, Nagao T et al (1993) Surface phonon dispersion curves of $NiA_l(111)$. Jpn J Appl Phys 32:3252–3256. https://doi.org/10.1143/JJAP.32.3252

[10] Hossain FM, Riley DP, Murch GE (2005) Ab initio calculations of the electronic structure and bonding characteristics of LaB_6. Phys Rev B Condens Matter Mater Phys. https://doi.org/10.1103/PhysRevB.72.235101

[11] Zhou X, Zhang H, Cheng C et al (2009) First-principles study of structural, electronic and elastic properties of diboride of vanadium. Phys B Condens Matter 404:1527–1531. https://doi.org/10.1016/j.physb.2009.01.013

[12] Otani S, Nakagawa H, Nishi Y, Kieda N (2000) Floating zone growth and high temperature hardness of rare-earth hexaboride crystals: laB_6, CeB_6, PrB_6, NdB_6, and SmB_6. J Solid State Chem 154:238–241. https://doi.org/10.1006/jssc.2000.8842

[13] Otani S, Tanaka T, Ishizawa Y (1993) Crystal quality and high temperature hardness of LaB_6 crystals prepared by the floating zone method. J Alloys Compd. https://doi.org/10.1016/0925-8388(93)90506-I

[14] Takagi K, Ishii M (1977) Growth of LaB_6 single crystals by a laser heated floating zone method. J Cryst Growth 40:1–5. https://doi.org/10.1016/0022-0248(77)90025-2

[15] Motojima S, Takahashi Y, Sugiyama K (1978) Chemical vapor growth of LaB_6 whiskers and crystals having a sharp tip. J Cryst Growth 44:106–109. https://doi.org/10.1016/0022-0248(78)90333-0

[16] Kher S, Spencer JT (1998) Chemical vapor deposition of metal borides 7. The relatively low temperature formation of crystalline lanthanum hexaboride thin films from boron hydride cluster compounds by chemical vapor deposition. J Phys Chem Solids 59:1343–1351. https://doi.org/10.1016/S0022-3697(97)00230-8

[17] Hasan M, Sugo H, Kisi E (2013) Low temperature carbothermal and boron carbide reduction synthesis of LaB6. J Alloys Compd 578:176–182. https://doi.org/10.1016/j.jallcom.2013.05.008

[18] Yuan Y, Zhang L, Liang L et al (2011) A solid-state reaction route to prepare LaB_6 nanocrystals in vacuum. Ceram Int 37:2891–2896. https://doi.org/10.1016/j.ceramint.2011.03.073

[19] Zhang M, Yuan L, Wang X et al (2008) A low-temperature route for the synthesis of nanocrystalline LaB_6. J Solid State Chem 181:294–297. https://doi.org/10.1016/j.jssc.2007.12.011

[20] Ağaoğulları D, Duman İ, Öveçoğlu ML (2012) Synthesis of LaB_6 powders from La_2O_3, B_2O_3 and Mg blends via a mechanochemical route. Ceram Int 38:6203–6214. https://doi.org/10.1016/j.ceramint.2012.04.073

[21] Ağaoğullari D, Balcı Ö, Öveçoğlu ML, Duman İ (2016) Preparation of LaB_6 powders via calciothermic reduction using mechanochemistry and acid leaching. KONA Powder Part J 2016:203–218. https://doi.org/10.14356/kona.2016001

[22] Gilman PS, Benjamin JS (1983) Mechanical alloying. Annu Rev Mater Sci 13:279–300. https://doi.org/10.1146/annurev.ms.13.080183.001431

[23] Suryanarayana C, Ivanov E, Boldyrev VV (2001) The science and technology of mechanical alloying. Mater Sci Eng, A 304–306:151–158. https://doi.org/10.1016/S0921-5093(00)01465-9

[24] Suryanarayana C (2001) Mechanical alloying and milling. Prog Mater Sci 46:1–184. https://doi.org/10.1016/S0079-6425(99)00010-9

[25] Benjamin JS (1990) Mechanical alloying—a perspective. Met Powder Rep 45:122–127. https://doi.org/10.1016/S0026-0657(10)80124-9

[26] Hadef F, Otmani A (2015) Mechanical alloying/milling. In: Handb Mech Nanostructuring, pp 263–276

[27] Sritharan T, Boey FYC, Srinivas A (2007) Synthesis of complex ceramics by mechanochemical activation. J Mater Process Technol 192–193:255–258. https://doi.org/10.1016/j.jmatprotec.2007.04.079

[28] Suryanarayana C, Ivanov E (2013) 3—Mechanochemical synthesis of nanocrystalline metal powders. In: Adv Powder Metall, pp 42–68

[29] Balcı Ö, Ağaoğulları D, Öveçoğlu ML, Duman İ (2016) Synthesis of niobium borides by powder metallurgy methods using Nb_2O_5, B_2O_3 and Mg blends. Trans Nonferrous Met Soc China (English Ed 26:747–758. https://doi.org/10.1016/s1003-6326(16)64165-1

[30] Aĝaoĝullari D, Gökçe H, Duman I, Öveçoĝlu ML (2012) Characterization investigations of ZrB 2/ZrC ceramic powders synthesized by mechanical alloying of elemental Zr, B and C blends. J Eur Ceram Soc 32:1447–1455. https://doi.org/10.1016/j.jeurceramsoc.2011.04.026

[31] Akgün B, Çamurlu HE, Topkaya Y, Sevinç N (2011) Mechanochemical and volume combustion synthesis of ZrB_2. Int J Refract Met Hard Mater 29:601–607. https://doi.org/10.1016/j.ijrmhm.2011.04.005

[32] Khaghani-Dehaghani MA, Ebrahimi-Kahrizsangi R, Setoudeh N, Nasiri-Tabrizi B (2011) Mechanochemical synthesis of Al_2O_3–TiB_2 nanocomposite powder from Al–TiO_2–H_3BO_3 mixture. Int J Refract Met Hard Mater 29:244–249. https://doi.org/10.1016/j.ijrmhm.2010.11.001

[33] Yeh CL, Li RF (2009) Formation of TiB_2–Al_2O_3 and NbB_2–Al_2O_3 composites by combustion synthesis involving

thermite reactions. Chem Eng J 147:405–411. https://doi.org/10.1016/j.cej.2009.01.007

[34] Mishra SK, Das SK, Pathak LC (2006) Sintering behaviour of self-propagating high temperature synthesised ZrB2-Al2O3 composite powder. Mater Sci Eng a-Structural Mater Prop Microstruct Process 426:229–234. https://doi.org/10.1016/j.msea.2006.04.026

[35] Jianxin D, Xing A (1997) Wear resistance of Al2O3/TiB2 ceramic cutting tools in sliding wear tests and in machining processes. J Mater Process Technol 72:249–255. https://doi.org/10.1016/S0924-0136(97)00176-3

[36] Mishra S, Rupa P, Das S, Shcherbakov V (2007) Effect of titanium diluent on the fabrication of Al_2O_3–ZrB_2 composite by SHS dynamic compaction. Compos Sci Technol 67:1734–1739. https://doi.org/10.1016/j.compscitech.2006.05.014

[37] Williamson G, Hall W (1953) X-ray line broadening from filed aluminium and wolfram. Acta Metall 1:22–31. https://doi.org/10.1016/0001-6160(53)90006-6

[38] Lu L, Lai MO, Zhang S (1997) Diffusion in mechanical alloying. J Mater Process Technol 67:100–104. https://doi.org/10.1016/S0924-0136(96)02826-9

[39] Chauruka SR, Hassanpour A, Brydson R et al (2015) Effect of mill type on the size reduction and phase transformation of gamma alumina. Chem Eng Sci 134:774–783. https://doi.org/10.1016/j.ces.2015.06.004